Analysis of ballistic waves in seismic noise monitoring of water table variations in a water field site: added value from numerical modelling to data understanding

S. Garambois, C. Voisin, M Romero guzman, D Brito, B. Guillier, A. Refloch

Geophysical Journal International

Geophys. J. Int. (2019) **219,** 1636–1647
Advance Access publication 2019 September 02
GJI Marine Geosciences and Applied Geophysics

doi: 10.1093/gji/ggz391

Analysis of ballistic waves in seismic noise monitoring of water table variations in a water field site: added value from numerical modelling to data understanding

S. Garambois,[1] C. Voisin,[1] M.A. Romero Guzman,[1] D. Brito,[2] B. Guillier[1] and A. Réfloch[3]

[1] *Université Grenoble Alpes, Univ. Savoie Mont Blanc, CNRS, IRD, IFSTTAR, ISTerre, UMR* 5275, 38000 *Grenoble, France. E-mail: Stephane.Garambois@univ-grenoble-alpes.fr*
[2] *Univ. Pau & Pays Adour, /TOTAL/CNRS, Laboratoire des Fluides Complexes et leurs Réservoirs - IPRA, UMR* 5150, *Pau, France*
[3] *Métropole de Lyon, Direction de l'Eau et des Déchets, Eau potable,* 20 *rue du Lac,* 69003 *LYON, France*

Accepted 2019 August 30. Received 2019 March 15; in original form 2019 August 13

SUMMARY

Passive seismic interferometry allows to track continuously the weak seismic velocity changes in any medium by correlating the ambient seismic noise between two points to reconstruct the Green's function. The ballistic surface waves of the reconstructed Green's functions are used to monitor the changes of water table induced by a controlled experiment in the Crépieux-Charmy (France) exploitation field. Viscoelastic numerical modelling of the monitoring experiment reproduces quite satisfactorily the sensitivity of the surface waves to the water table previously observed with seismic noise data. This numerical approach points out that this sensitivity is controlled by mode mixing of Rayleigh waves. It also made it possible to identify the refracted *P* wave and to extract its anticorrelated sensitivity to water table variations. Depending on the offset between receivers, it was observed numerically that the interferences between the different waves (with different velocities) composing the seismic wavefield slightly affect the quantitative sensitivity to water table changes. This suggests the use of an optimal spatial and temporal observation window for which wave interference is minor and does not blur the quantitative response to water table variations. We were thus able to determine the relationship between velocity and water table variations for all waves involved. From numerical computations, we identify a weak signal-to-noise ratio phase in the noise correlograms, with a anticorrelated sensitivity to the water table: the reconstructed refracted waves.

Key words: Hydrogeophysics; Numerical modelling; Seismic interferometry; Seismic noise; Wave propagation.

1 INTRODUCTION

Geophysics offers many techniques for detecting, characterizing and monitoring the fluids and their migration in the Earth's crust over a large spectrum of spatial and temporal scales. Among them, active seismic methods proved their efficiency in high-resolution time-lapse imaging for reservoir management (Bianchi *et al.* 2004) or to detect, quantify or monitor near-surface water content (Garambois *et al.* 2002; Pasquet *et al.* 2015), notably using Biot-Gassmann theory (Biot 1962). Although promising, these active seismic techniques require heavy logistics difficult to implement in terms of source and receivers management that only the oil industry can afford particularly when large time and space scales are considered. Alternative techniques based on the continuous recording of seismic noise have been developed for almost 20 yr (Lobkis & Weaver 2001). The basic principle inherent in these methods is that the Earth response to perturbations between two points (Green's function) can be reconstructed by cross-correlating the two seismic noise records if noise sources are isotropically distributed (Campillo & Paul 2003). The monitoring potential of these techniques was first evidenced on the Merapi volcano by using late coda waves and by quantifying their weak velocity variations generated by weak changes of the poroelastic properties related to precipitations and changes of the water table (Sens-Schoenfelder & Wegler 2006). As suggested by Larose *et al.* (2015), the ambient seismic noise should be used to monitor environmental processes involved in the hydrosphere. Voisin *et al.* (2016) recorded pore pressure perturbations expressed in velocity changes computed from ballistic waves on an active landslide in New Zealand. Using a poroelastic model, they showed that the surface waves velocity variations were linked to water table changes. They successfully reproduced the amount of surface waves velocity change as well as the frequencies where

occurred these velocity variations. Voisin *et al.* (2017) used the same approach to monitor the water table variations generated by a controlled drain/filling basin cycle within a groundwater exploitation field, and introduced the concept of virtual piezometer. Recently, Fores *et al.* (2018) combined ambient seismic noise and gravimetry measurements to monitor saturation changes at larger depth in karstic formations. On a larger scale, both Tsai (2011), Lecocq *et al.* (2017) or Clements & Denolle (2018) suggest that seismic noise based methods allow to monitor and locate the hydrological variations within the unsaturated layer and also the interface with the saturated zone. The Green's function is formed of ballistic waves (*P*, *S*, surface waves) followed by coda waves (multiply diffracted in the medium). All these waves have different sensitivities to water and may interfere under certain conditions of distance and time window selection used for the velocity variation retrieval. Such interference may lead the misinterpretation of velocity changes in terms of groundwater changes. In this paper, we deal with velocity variations derived from seismic noise cross-correlation between two seismic stations in a water exploitation field (Voisin *et al.* 2017). The water field, located within the metropole of Lyon (France), provides access to controlled pumping/filling experiments as well as to the associated piezometric data (Loizeau 2013; Réfloch 2018). After presenting the field test site and the results of the seismic monitoring obtained during a drain/filling cycle of a basin, we show how we establish a 1-D stratified viscoelastic model by combining active seismic measurements and Biot–Gassmann fluid substitution poroelastic modelling. It allows notably to identify the different wave types present in the seismogram. Then, we simulate the seismic wave propagation for different groundwater levels to obtain a synthetic correlogram of the drain/filling cycle, which is consistent in waveforms with the experimental one. We reproduce the seismic velocity variations driven by the water table depth variations as deduced from the seismic noise measurements. The seismograms computed with 200 offsets help to identify the different waves and to study their respective sensitivity to water table depth variations. Comparing the synthetic correlogram with the real correlogram, we identify different seismic phases of interest for water table monitoring: a refracted wave and different modes of Rayleigh waves, which have opposite sensitivities to water table variations. The distance between the seismic stations as well as the selected time window used for velocity variation computations are crucial parameters. Indeed, as the velocity sensitivity of each wave type differs, there is an optimal offset window which must be taken into consideration to avoid wave interference and to properly extract the water table variations. The quantitative relationship between velocity variations and corresponding water table depths are established for each wave.

2 SEISMIC INVESTIGATIONS AROUND THE INFILTRATION BASIN

2.1 The Crépieux–Charmy water exploitation field site

The Crépieux–Charmy water exploitation field is located in the alluvial plain of the Rhône River, Northeast of Lyon, the second largest city of France. The Eastern aquifer of Lyon is a free aquifer characterized by glacio-fluvial Würmien deposits composed of a sequence of low-permeability Pliocene glacial claystones and molasses covered by recent alluvial deposits of high-permeability estimated around 10^{-3} m s^{-1}. The latter forms a sandy-gravel size grain sedimentary sequence with a heterogeneous distribution and a 10–25 m thickness (Loizeau 2013).

The preserved area reaches up to 375 ha and produces about 85 per cent of the drinkable water needs of Lyon Metropole (1.3 million inhabitants). This represents an average production of 210 000 m^3 d^{-1}. The area is equipped with 111 pumping wells and 12 infiltration basins designed to prevent potential groundwater pollution by modification of underground fluids flows and to recharge the groundwater (Fig. 1a).

The experiment described here is focused on the functioning of the basin 5-2 (Fig. 1) equipped with piezometers P95 and P96, that have been found to be close to the maximum of the hydraulic dome formed during the infilling of the basin (Voisin *et al.* 2017). Ten vertical seismometers (5 Hz) were deployed around the basin 5-2 to record the ambient seismic noise before, during and after a drain/filling cycle, but only worked properly during the experiment.

2.2 Seismic noise monitoring results

In practice, ambient noise is recorded for many hours, days or months depending on observation purposes. Noise traces are correlated over short time windows and then averaged (Schuster 2009). Seismic noise cross-correlated results, denoted correlograms, are generally represented as a function of monitor time and show series of waves arriving at different propagation times. These arrival times slightly changing with the changes of groundwater table are able to detect tiny seismic wave velocity variations induced for instance by groundwater changes (Sens-Schoenfelder & Wegler 2006; Voisin *et al.* 2016).

From 26 April to 5 May of 2017, nine 5-Hz vertical geophones (Fig. 1) placed around basin 5-2 recorded the seismic noise wavefield with a sampling frequency of 250 Hz (Fig. 1b). During this acquisition, an hydraulic barrier was generated by filling the basin 5-2 with water and creating a dome-shaped water table (Voisin *et al.* 2017). The piezometric level is recorded by the P96 piezometer every 10 min (Fig. 1b), displaying a maximum variation of 3 m of the piezometric level.

Cross-correlations are computed between all pairs of stations every hour (Voisin *et al.* 2017). This choice of time sampling is the result of a compromise between obtaining a good signal-to-noise ratio while ensuring a fair hydrodynamic reconstruction of the experiment. Here, we are focused on the pair of stations 5 and 6 (offset of 168 m) given that P96 piezometer is exactly between these two receivers. The first 3 s of the causal part of the correlogram are shown on Fig. 2(a) and correspond to ballistic waves travelling from station 5 towards station 6. The main local noise sources are the rivers and channels, the railway and the highway. We verified that the structure of the noise is quite stable both in space and time at least until 60 Hz, allowing a reliable monitoring of the variations of the medium. During the hydraulic barrier activation, an additional noise source is related to the infilling of the basin, which results in an apparent change of amplitude of the waveforms between 120 and 140 hr of monitoring time (Fig. 2a).

The correlogram is dominated by large amplitude of low frequency phases arriving between 0.5 and 1.1 s of time lag. A higher frequency phase, which is above the noise, also emerges around a time lag of 0.4 s. All these events are part of the ballistic waves travelling from station 5 to 6. These reconstructed arrivals are continuous over the whole seismic noise acquisition and so can be used to monitor the subsoil. Indeed, changes of arrival time of these ballistic waves are clearly visible. The stretching technique (Sens-Schoenfelder & Wegler 2006) can be used to precisely measure time delays compared to a reference obtained by averaging the whole

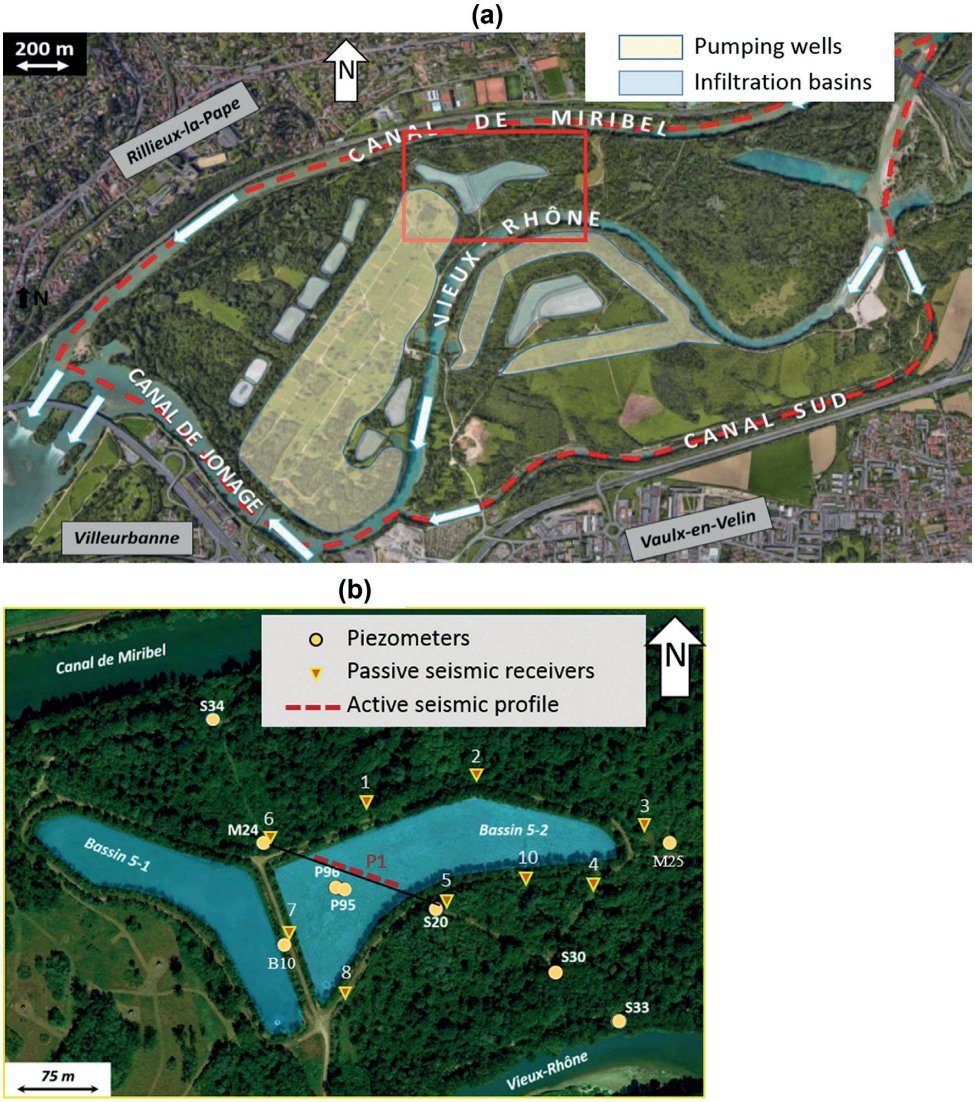

Figure 1. (a) Aerial view of the Crépieux-Charmy site bounded by three channels (Canal Sud, Canal de Miribel and Canal de Jonage). White arrows display the rivers stream. The location of the studied basins zoomed in (b) is indicated by the red rectangle. (b) Infiltration basins 5-1 and 5-2 with selected piezometers (yellow dots), passive receivers (orange triangles) and the active seismic profile (dashed red lines) performed when the basin was dry.

set of correlations (Fig. 2b). Assuming that the relative velocity changes dv/v are laterally homogeneous between the two sensors, these relative time delays are expressed as $\delta t/t = -\mathrm{d}v/v$ (Grêt *et al.* 2006; Sens-Schoenfelder & Wegler 2006). In our case, the relative velocity changes, corresponding to the real velocity changes as the source distribution is relatively homogeneous in space, are computed accordingly after selecting time windows corresponding to the most energetic seismic phases (red bar in Fig. 2b), without prior knowledge of their nature. Fig. 2(c) shows the smoothed relative velocity variations derived between station pair 5–6 (red curve) as well as the concomitant relative water table variations (blue curve) measured at P96 piezometer. This result and the generalization to all station pairs (Voisin *et al.* 2017) highlight a clear anticorrelation between water table variations and dv/v computed from seismic noise. These experimental results show a direct application of seismic noise recording for water table monitoring in urban and water exploitation context.

3 SEISMIC WAVE PROPAGATION MODELLING

3.1 Derivation of a 1-D viscoelastic model from active measurements

The understanding of the seismic noise observations requires a wave propagation numerical study using a model representative of the site. For its establishment, an active seismic survey has been conducted along transect P1 located between the studied station pair 5–6 (Fig. 1b).

The acquisition was composed of 48 4.5 Hz vertical geophones connected to a Geode acquisition system of Geometrics. A stack of vertical hammer shots on a plate generates *P* and vertically polarized shear waves (*P*–SV), as displayed on Fig. 3(a) for the shot located at an offset $x = 0$ m. The seismogram has an energy mainly confined in the [15–70 Hz] frequency range. All records are dominated by strong amplitude low frequency waves, although weak volume waves composed of direct, refracted and reflected arrivals appear

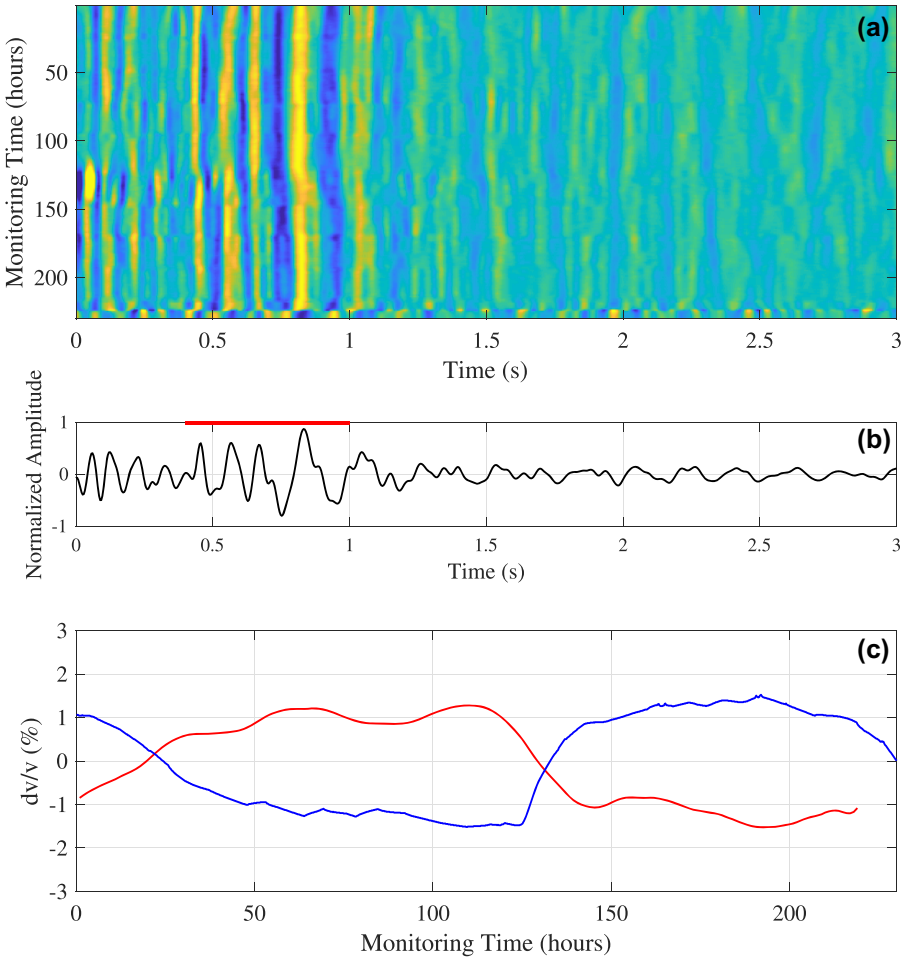

Figure 2. (a) Correlogram between stations 5 and 6 (offset of 168 m). The seismic data are filtered in the 3–40 Hz frequency range. They are cut into 1 hr windows and whitened in the spectral domain before correlation. (b) Stack of all correlations of the correlogram (a). The red bar indicates the time window chosen for the velocity variation estimates and includes the most energetic phases. (c) Relative water table variations (blue curve) and dv/v (red curve) computed over the 0.4–1 s time window. Note that velocity changes are anticorrelated to the water table variations.

earlier. The onset of first arrivals (direct and refracted waves) are inverted using the Simultaneous Iterative Reconstruction Technique (Dines & Lyttle 1979) implemented in a 3-D software designed for velocity tomography analysis (Demanet *et al.* 2001). The *P*-wave tomography (Fig. 3b) shows a main large contrast at 5 m depth, which corresponds to the water table (measured at a depth of 5.1 m by P96 piezometer at the time of the seismic acquisition). A weaker contrast also appears at 11 m depth. The velocity distribution shows weak variations along the profile, thus suggesting that the medium is vertically stratified. A multiple Analysis of the Surface Waves (MASW) has been done using the linear-FK Tool integrated in the Geopsy package (Wathelet *et al.* 2004), providing a semblance map of the velocity and frequency of the waves travelling with the highest energy (Fig. 3c). This FK map computed between 10 and 120 Hz shows that the most energetic waves are composed of two Rayleigh modes, the fundamental and the first higher mode, which are relatively well separated on the FK map. The first higher mode, which exhibits larger dispersion properties than the fundamental one, was picked between 16 and 36 Hz and then inverted with the Geopsy/Dinver package (Wathelet *et al.* 2004) that uses a neighbourhood algorithm optimization method. This method is a stochastic direct search method to find models with acceptable fit with the observed data within a multidimensional parameter space (Sambridge 1999a,b). We obtain thousands of *S*-wave velocity profiles, those with the best fits are shown in red on Fig. 3(d). They all converge towards a three layer model, that highlights a superficial soft layer at 1.5 m depth ($Vs = 150$ m s^{-1}) overlying a 8–10 m thick 300 m s^{-1} layer (Vs) layer which stay on a high velocity layer ($Vs > 900$ m s^{-1}). This deeper contrast is consistent with observations coming from the P96 borehole, that give the passage to claystones at 11 m depth. The presence of the water table could not be identified directly from the surface wave analysis. It must be noted that a transverse acquisition, performed with transverse shots and geophones, show consistent results with Rayleigh wave inversion and also allowed to verify that a large refracted *S* wave is coincident with the wave arriving at about 180 ms at an offset of 72 m (Fig. 3a). Consequently, this rather large event has been interpreted as a refracted *S* wave on the claystone layer, which is also well visible at higher frequencies on Fig. 3(c).

3.2 Influence of the water table using a poroelastic model

The influence of the water table on seismic velocities is adressed using a Biot–Gassmann multiphasic poroelastic approach (Dupuy *et al.* 2015). While the extreme velocity values (dry or saturated environments) provided by such a model are generally considered

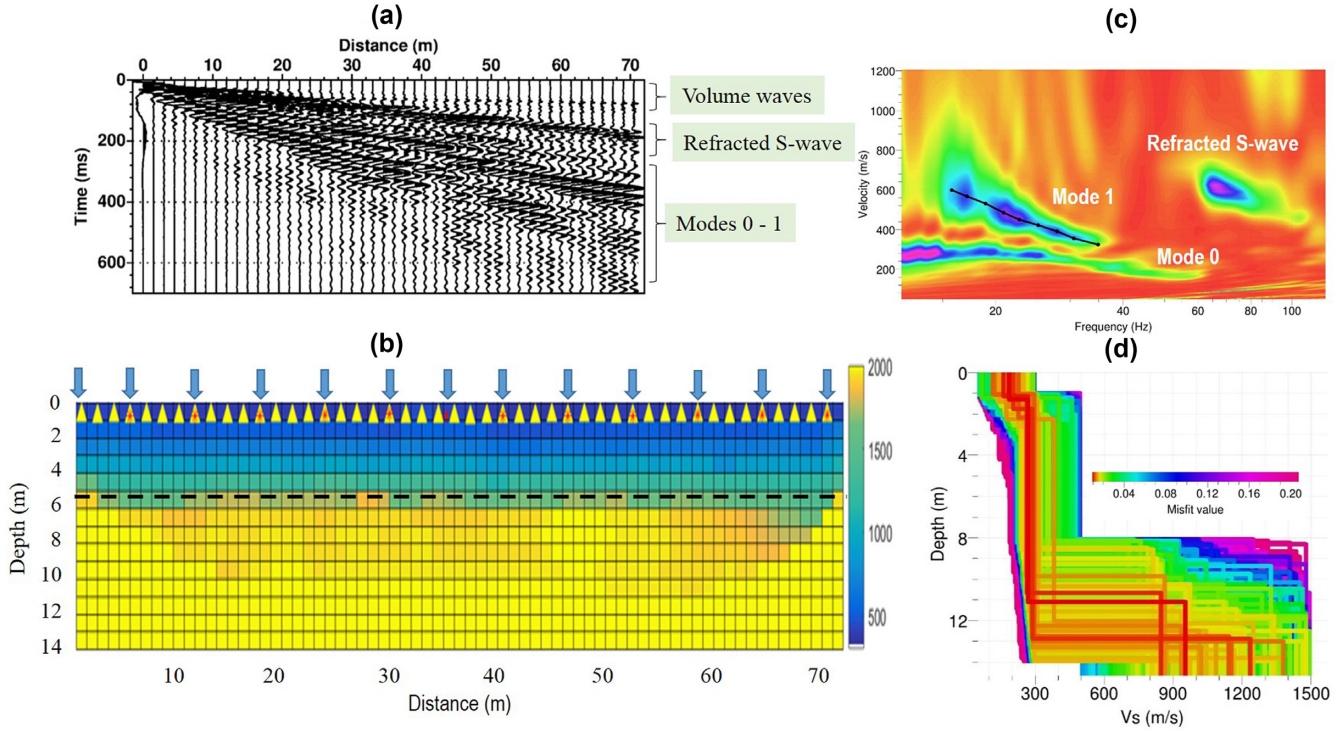

Figure 3. (a) Stack of active recordings in basin 5-2 using a vertical source (hammer) and 48 vertical geophones (1.5 m spacing). The main events are identified as refracted and reflected volume weak waves, followed by a refracted *S* wave and then by a mixture of the fundamental and first modes of Rayleigh waves. (b) *P*-wave velocity distribution within basin 5-2 (when emptied) obtained from tomography inversion of first arrival onsets considering several shots (blue arrows) and several receivers (triangles). The dashed black line represents the water table location at the time of the acquisition. (c) Semblance map of phase velocity versus frequency for the seismogram displayed in (a) showing the dispersion properties of two well-separated Rayleigh modes. (d) *S*-wave velocity profiles obtained after inversion of the first higher mode of Rayleigh waves.

reliable, several laws are possible to reproduce the *P*-wave velocity sensitivity to partial saturation and this law should be used with caution in this case. The modelling requires a value for the porosity that is set up to 45 per cent and corresponds to very permeable coarse alluvial deposits. The frame compressibility and shear modulus are calibrated from the measured dry seismic velocities of 800 m s^{-1} for *P* waves and 300 m s^{-1} for *S* waves, which were derived from active measurements. The Biot–Gassmann sensitivity of seismic velocities to water saturation shows that *P*-wave velocity displays a large increase from 800 to 1800 m s^{-1} when increasing water saturation (Fig. 4a). At the same time, *S*-wave velocity decreases almost linearly from 300 to 250 m s^{-1} (Fig. 4a). By incorporating these sensitivity results with those derived from active seismic measurements and borehole observations, we constructed a viscoelastic model that is broadly consistent with all the information. This viscoelastic model, displayed in Fig. 4(b), consists of three layers: (i) a 1.5-m-thick soft layer with very low seismic velocities representing very recent basin deposits (ii) a 9.5-m-thick homogeneous highly permeable gravel layer in which velocities vary over time according to the water table changes and (iii) a compact claystone layer appearing at 11 m depth with a large *S*-wave seismic velocity. In addition, the effect of the water table has been modelled as an interface between dry and saturated gravels, whose depth will mimic piezometric measurements. It must be noted that attenuation properties are assumed homogeneous for all layers and do not vary with water table variations.

3.3 Identification of waves using viscoelastic modelling

The seismograms are computed using a 3-D code modelling seismic wave propagation in a plane-layered viscoelastic isotropic medium excited by point sources (Dietrich 1988), extended for seismo-electromagnetic wave studies in poroelastic media (Garambois & Dietrich 2002). The code is based on the generalized reflection and transmission matrix method of Kennett & Kerry (1979) and uses the discrete wavenumber integration method of Bouchon (1981). This approach, which allows to compute partial solutions at each interface, suffers from not being able to take into account lateral heterogeneities or diffracting points. It computes the pressure and the three components of the particle displacements in the three directions. The source is a zero-phase Ricker wavelet time dependent with adjustable peak frequency. The particle velocity is obtained after a time derivation of the displacements. One of the advantages of this generalized reflectivity formalism lies in the possibility of computing partial solutions by omitting the free surface and/or reflections at any given interface.

Two hundreds synthetic geophones, separated by 3 m, are aligned along the *x*-axis from 3 to 600 m of offsets at a depth $z = 50$ cm (Fig. 5a). A vertical seismic source is placed at $x = 0$ m. The choice of the source frequency has been chosen in accordance with the spectral content of the experimental correlogram, which is dominated by ballistic waves propagating between 5 and 8 Hz (Fig. 2a). The particle velocity is modelled with the derivative of a Ricker pulse. The seismograms presented in Fig. 5 have been computed using the model shown in Fig. 4(b) with a water table interface located at 5.1 m depth. A constant arbitrary quality factor $Q_P = Q_S =$

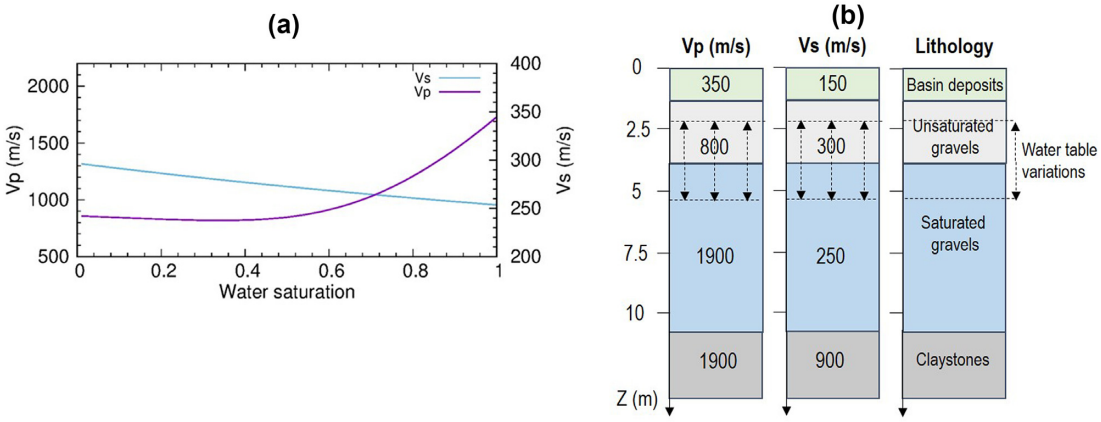

Figure 4. (a) Poroelastic sensitivity curves of *P* (purple) and *S* (blue) seismic velocities according to water saturation for a geological layer with 45 per cent of porosity. (b) Seismic velocity models chosen to compute synthetic seismograms. They represents coarse lithological and hydrological variations of the subsurface, the deepest claystone layer being assumed as a high *S*-wave velocity half-space.

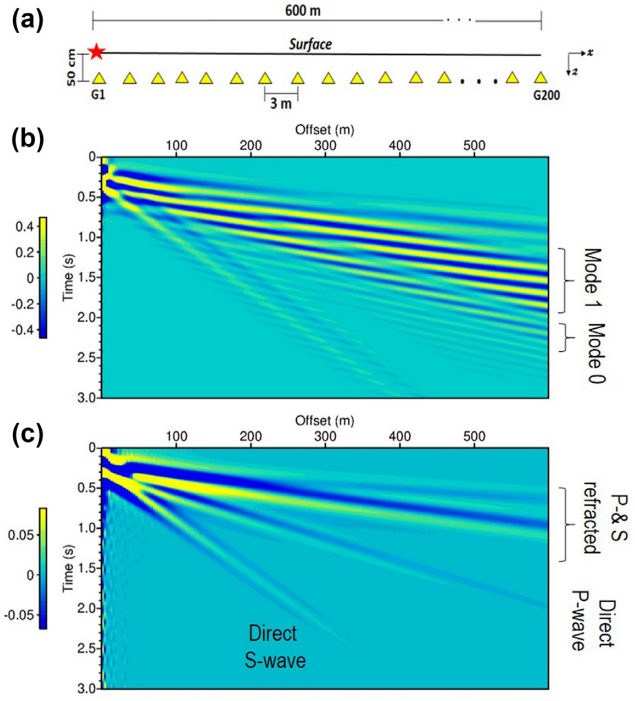

Figure 5. (a) Layout of the numerical experiment using 200 geophones located every 3 m at a constant 50 cm depth with a vertical seismic sources located nearby the surface. (b) Vertical velocity seismogram obtained from the layout of (a). The record is dominated by multimodes Rayleigh waves. (c) Same as (b) but omitting the free surface. The record is dominated by volume waves.

100 was chosen to reproduce the attenuation, but this parameter does not have much influence on the results as long as it is restricted within a reasonable range corresponding to sediments. Fig. 5(b) shows that the low frequency content of the source signal in this near-surface context induces a significant mixing of different waves especially at small offsets, with a lot of interferences. To better identified the composition of the wavefield, a synthetic modelling has been computed by omitting the free surface (Fig. 5c), showing the weak amplitude of the direct and refracted *P* and *S* waves. When the free surface condition is added (Fig. 5b), the wavefield is dominated by multimodes Rayleigh waves, poorly separated in the time domain, which exhibit an amplitude five times higher than the volume waves, the same proportion as observed on the shot recording (Fig. 3a). It has been numerically verified that the large amplitude of these waves is due to the presence of the clay layer at 11 m depth, which generates a very high contrast of *S*-wave velocity and consequently large multimode Rayleigh waves. The first higher mode spreads faster than the fundamental mode, as displayed on Fig. 5(b) and the relative amplitude of both modes vary according to offset, the first higher mode becoming dominant for offsets larger than 250 m. Finally, as displayed in Fig. 5(c), the very low frequency content of our simulations, chosen to reproduce the spectral content of the experimental correlogram, prevents a very clear separation of the different *P*, *S* refracted waves and surface waves arriving at short times, particularly at short offsets where they would interfere.

4 DERIVATION AND ANALYSIS OF A SYNTHETIC CORRELOGRAM

The cross-correlation of signals acquired between two stations A and B is formed by the propagation of waves from A to B (causal part; receiver A is turned in a virtual seismic source recorded in B); and from B to A (anticausal part; receiver B is turned in a virtual seismic source recorded in A). Any change on the water level depth affects the waveforms of the waves propagating between the two stations A and B. In order to reproduce the seismic noise monitoring experiment, we use the hourly water table variations measured in the P96 piezometer to generate 230 viscoelastic models differing only by the depth of the water table.

4.1 Comparison between numerical and field data results

Fig. 6 a shows the synthetic correlogram obtained for the trace located at an offset of 168 m, that is the same distance separating stations 5 and 6 in the experience. It was obtained by gathering the 230 simulations that reproduce the hourly water table depths as measured by the P96 piezometer during the seismic noise experiment,ranging from 2.4 to 5.4 m. The synthetic correlogram shows a good agreement with respect to the correlogram derived from the seismic noise experiment (Fig. 2a), but of course less noisy. Indeed, the sequence of arrivals is the same with consistent kinematics and relative amplitudes. Both correlograms are dominated by a maximum amplitude wave arriving between 0.6 and 1 s, although a

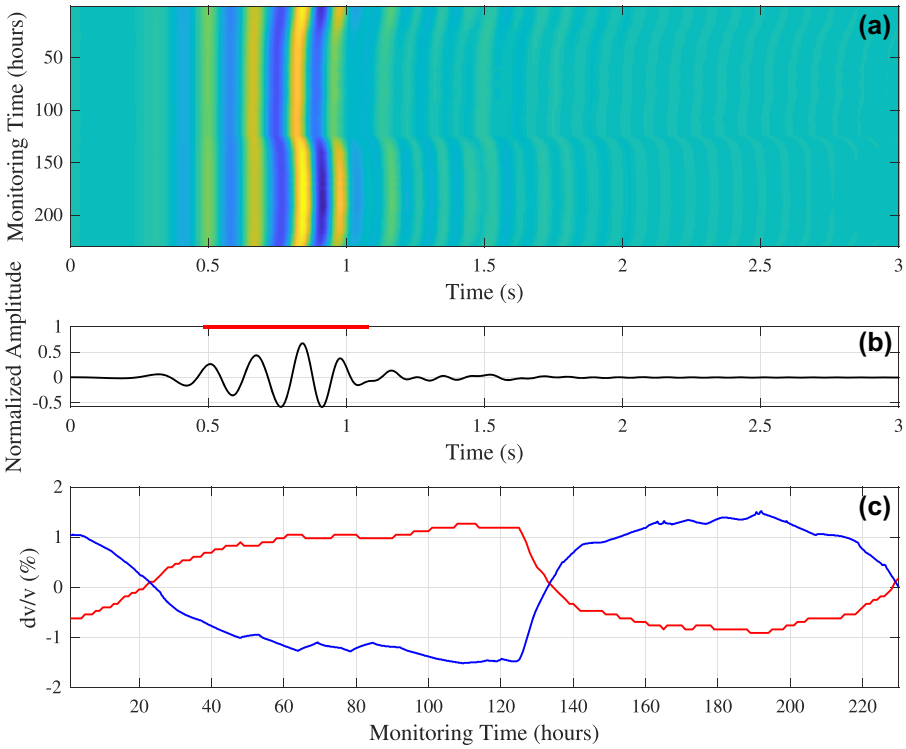

Figure 6. (a) Synthetic waveform variations (equivalent to a synthetic correlogram) of trace located at an offset of 168 m over the 230 hr of water table monitoring. (b) Reference trace resulting from the stack of all traces present in the correlogram (a). The red bar indicates the time window chosen for the analysis. (c) dv/v (red curve) and relative water table variations (blue curve). The velocity changes are computed over the 0.5–1.1 s time window that includes the most energetic waves present in the correlogram.

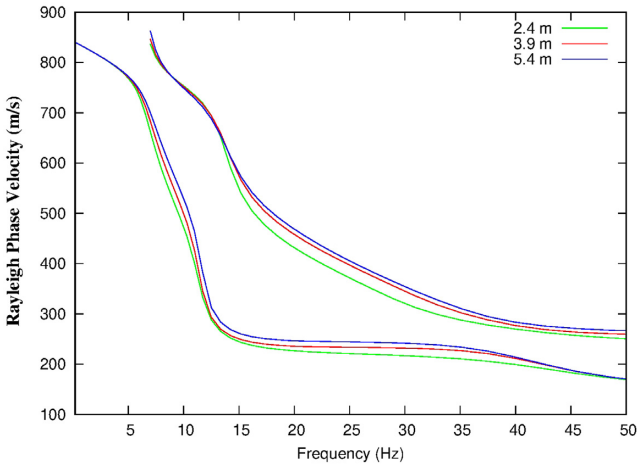

Figure 7. Dispersion curves for fundamental and first higher Rayleigh modes computed based on the layered subsoil model presented in Fig. 4(b) for three specific water levels as measured on P96 piezometer: the shallower at 2.4 m depth (green), the average at 3.9 m depth (red) and the deepest one at 5.4 m depth (blue).

weaker arrival can also be observed before 0.5 s. For this offset and in the 0.6–1.1 s time window, Fig. 5(b) shows that the two identified Rayleigh modes are not well separated and that their relative amplitudes are fairly balanced.

In both numerical and experimental cases, slight waveform variations due to water level changes (in blue in Fig. 6c) are directly visible. They appear slightly more pronounced when the water level rises around 130 hr of monitoring time in the synthetic case. The relative velocity variations dv/v are computed in the same way as was done for the seismic noise data, using the stretching technique within the same time window in which the most energetic waves are present, here between 0.5 and 1.1 s. The computations quantitatively reproduce the main result coming from the field experiment, where the relative velocity variations are inversely proportional to the relative water level variation: they are negative when water level goes up and are positive when water level goes down. This anticorrelation can only be explained by the anticorrelation of the *S*-waves velocity variations—and consequently of Rayleigh waves which dominate the time window—according to water saturation changes. This synthetic approach also replicates the order of magnitude of relative velocity variation which was observed during the field experiment, that is 1 per cent of relative velocity variation is a signature of roughly 1-m variation in groundwater level in this frequency range and lithological context.

As observed before, whether in active recordings (Fig. 3a), synthetic computations (Figs 5 b and 6) or seismic noise derived correlogram (Fig. 2a), Rayleigh waves appear to dominate the seismic wavefield. Therefore, the sensitivity of the Rayleigh waves to the water table variations seems to control the observed dv/v changes. To better quantify this effect, we computed the theoretical dispersion curves in the [0.2–50 Hz] frequency range for the fundamental and the first higher Rayleigh modes (Fig. 7) using the viscoelastic soil model derived from active measurements (Fig. 4b) for three specific water levels: (i) when the water table is very shallow at 2.4 m (green curve), when water table is very deep at 5.4 m (blue) and the average water table at 3.9 m (red). It should be noted that the theoretical dispersion curves are consistent with the one provided by the active shots in the frequency range [16–40 Hz] (Fig. 3c)

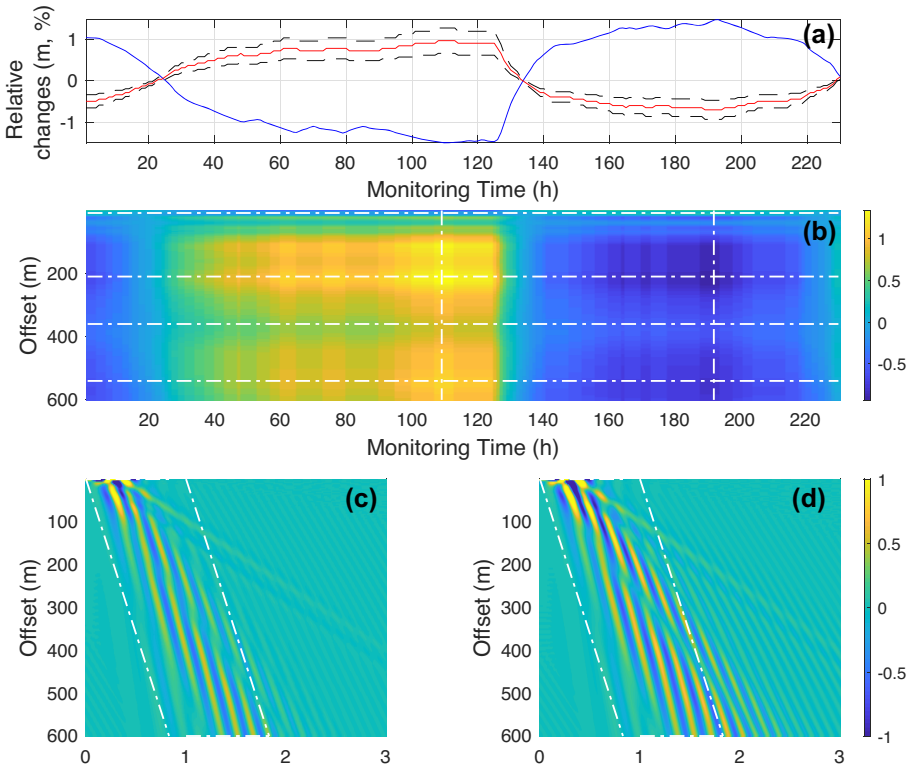

Figure 8. Synthetic analysis of the sensitivity of dv/v measurements versus offset for the dominant arrival. (a) Relative water table changes recorded at P96 piezometer (blue curve) and average synthetic d$v/v \pm 1\sigma$ (red and dashed black curves). Note the anticorrelation between both measurements. (b) Synthetic dv/v obtained for the different offsets measured on the dominant arrival [highlighted in white dashed line in plots (c) and (d)]. Note the changes of maximum and minimum amplitudes of dv/v with the offset. (c) The seismic wavefield at 109 hr (time of the lowest water table). In white dashed line, the time window used for computations of dv/v in plot (a) and (b). (d) The seismic wavefield at 192 hr (time of the highest water table). In white dashed line, the time window used for computations of dv/v in plot (a) and (b). The comparison of the seismic wavefield at the two times highlights the changes in the amplitude of the seismic waves alongside with a separation of the first two modes of Rayleigh waves at offset 400 m.

and that we can clearly observe the influence of each layer of the model, particularly of the fast claystones layer which generates a steep velocity increase of the fundamental Rayleigh mode in the low frequency range from 13 Hz.

Fig. 7 shows that both Rayleigh modes are sensitive to the water table depths, with higher velocities when the water table is deep (blue curve) and lower velocities when it is shallower. The velocity variations are in the order of a few percents, but they vary according to frequency and mode. In the [5–12 Hz] frequency range, variations are mainly controlled by the sensitivity of the fundamental Rayleigh mode. In the [12–45] Hz frequency band, the dispersion curves of both modes are very sensitive to water level variations. These observations indicate that the variations observed in the synthetic correlogram, whose spectral content is relatively narrow with little energy beyond 10 Hz, are mainly controlled by the fundamental Rayleigh mode. However, a part of the variations observed in the experimental correlogram, whose spectral content extends up to 20 Hz, could be due to the sensitivity of both Rayleigh modes. Fig. 7 also suggests that the relative variations in velocities to the water table are not symmetrical. Shallower the water table depth is, stronger is the impact on dispersion curves, especially for the higher Rayleigh mode. This could explain the larger variations observed in the experiment when the water table is shallower (Fig. 2c).

4.2 Offset dependency of dv/v measurements

As discussed previously, the most energetic phases reconstructed by cross-correlation are often assumed to correspond to the fundamental mode of Rayleigh waves. dv/v measurements made on these phases are classically interpreted with this assumption in mind in terms of depth sensitivity kernel. However, near surface applications might show a complex wavefield with higher modes of Rayleigh waves able to interfere with the fundamental mode. Fig. 8 highlights the impact of mode mixing on the dv/v measurement. We consider a moving time window adjusted to the traveltime of the prominent arrival indifferently. The average dv/v (Fig. 8a) is anti-correlated to the water table variation. The large uncertainties of 20 per cent shown by standard deviation of dv/v measurement (black dashed curves) are explained by the variations of dv/v according to offset (Fig. 8b). The composition of the seismic wavefield and the weight of each wave/mode entering the time window of interest is changing with offset, providing a different measurement of dv/v. On top of that dependency, the changes of the water table conditions affect the relative amplitudes of the different modes (Figs 8c and d), and this will affect the amplitude of dv/v too. Combined together, these effects degrade the precision of dv/v measurement up to 20 per cent which leads to a degraded estimate of the water table depth. A correct estimate of the water table with seismic noise measurements requires a good knowledge of the medium and a precise time window selection.

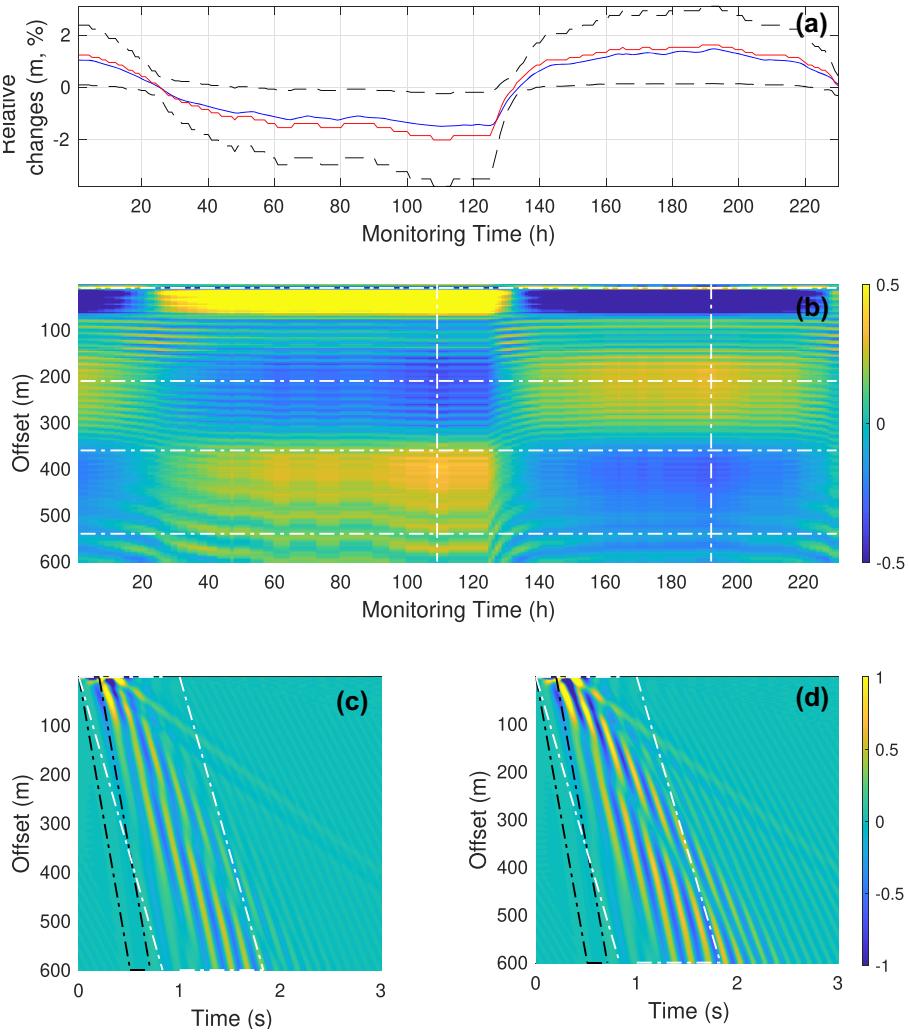

Figure 9. Synthetic analysis of dv/v measurements versus offset for the earlier arrivals. (a) Relative water table changes recorded at P96 (blue curve) and average over the 100–360 offset window of d$v/v \pm 1\sigma$ (red and dashed black curves, 10-fold increase). Note the positive correlation between both measurements. (b) dv/v derived for the different offsets measured on the time window (highlighted in black dashed line in plots (c) and (d), while the white dashed lines represents the time window selected when Rayleigh waves were considered). Note the changes of maximum and minimum amplitudes of dv/v with the offset. (c) The seismic wavefield at 109 hr (time of the lowest water table). In black dashed line, the time window used for computations of dv/v in plot (a) and (b). (d) The seismic wavefield at 192 hr (time of the highest water table). In black dashed line, the time window used for computations of dv/v in plot (a) and (b).

4.3 Monitoring the water table with reconstructed volume waves

A similar analysis of the dependency of dv/v with offset is achieved using a different time window containing only the first arrivals (Fig. 9), that is the direct and refracted *P* and *S* waves (black dashed box in Figs 9c and d). The main difference with Fig. 8 is the inversion of sensitivity of the dv/v measurement with the offset. From 100 to 360 m of offset, the dv/v measurement is correlated to the relative changes of water table because the *P* refracted wave dominates the time window of analysis for these offsets (Fig. 9a). At larger offsets, we observe a smooth transition to an anticorrelation between dv/v and the relative water table changes. This transition is related to a change of the nature of the wavefield within the time window of analysis, certainly due to the dominant presence of the refracted *S* wave at the claystone layer. Finally, we observe a fringe like pattern that alternates the sensitivity of dv/v from correlated to anticorrelated. These fringes arise from the presence of numerical noise inherent to the reflectivity method used for the computations.

The identification of the *P*-refracted wave in the model and the possibility to monitor the water table that it offers is of great interest. Going back to the data, we focus again on the pair of stations 5 and 6 with an offset of 168 m. In Fig. 2, we have shown the monitoring of the water table with the Rayleigh waves. Now we focus over the time window limited to the first arrivals (Fig. 10). Many arrivals with weak signal-to-noise ratios are present in the first 0.5 s of the causal part even at very small time lapse. This is inherent to the correlation of the seismic wavefield between two points: all waves arriving in phase at the two stations will correlate at near zero time lapse. Despite this complication, we identify a small time window (green bar in Fig. 10b) for which the dv/v presents a clear correlation with water table changes (Fig. 10c). This correlation is expected when *P* volume waves are dominant in a given time window, as shown from the poroelastic approach displayed in Fig. 4(a).

Fig. 11(a) presents the average sensitivity of the dv/v (mean $\pm\sigma$) to the water table changes when surface waves are considered. The average dv/v is a measurement made on the whole network of stations and is commonly used (Clements & Denolle 2018) to track

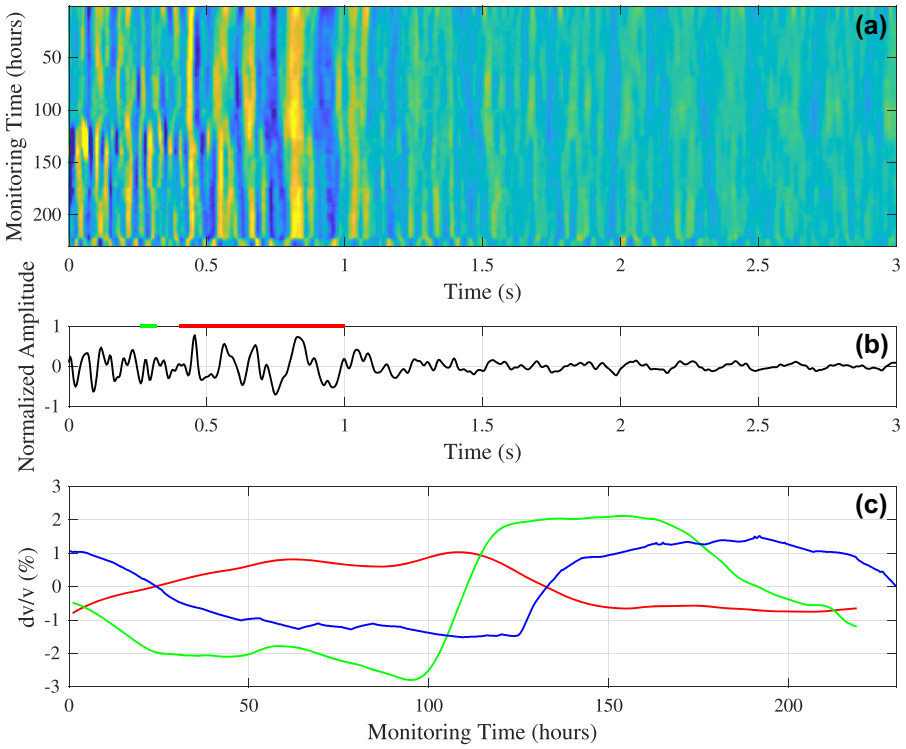

Figure 10. Station pair 5–6 (offset 168 m). (a) First 3 s of the causal part of the smoothed correlogram presented in Fig. 2(a). (b) Stack of the correlations over the 230 hr of the experiment. Red bar: dominant time window comprising the surface waves. Green bar: 'first arrival' time window, comprising the *P*-refracted wave. (c) Relative water table changes (blue curve), dv/v estimates based on the dominant time window (red curve) and the 'first arrival' time window (green curve). Note the correlation of the latter with the water table changes, a signature of the *P*-refracted wave.

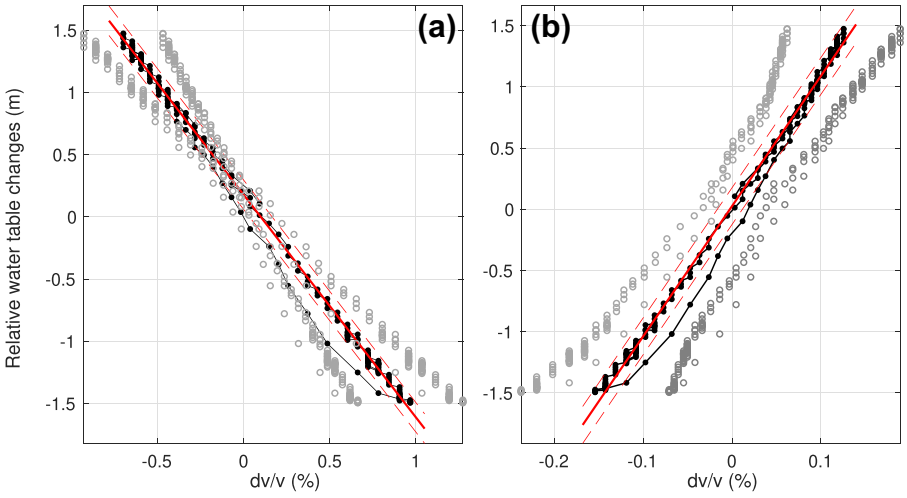

Figure 11. Relative water table changes recorded at P96 piezometer versus d$v/v \pm \sigma$ (black dots and grey circles respectively) for two different time windows used in the computation. (a) Measurements on the time window including mainly Rayleigh waves. Note the anti-correlation between the measurements, related to the sensitivity of *S*-wave velocity to water saturation. The red line represents the best linear fit to the data, with a slope of –1.072 ± 0.006. Intercept at the origin is 0.01188 ± 0.006. The dashed red lines are the 95 per cent confidence bounds. (b) Measurements made on the time window and offsets where only *P*-refracted waves are present (from 60 to 400 m). Note the correlation with the water table, related to the sensitivity of *P*-wave velocity to water saturation. The red line represents the best linear fit to the data, with a slope of 10.61 ± 0.1. Intercept at the origin is 0.025 ± 0.01. The dashed red lines are the 95 per cent confidence bounds.

the water table variations. Fig. 11(a) shows that the average dv/v sensitivity to the water table changes can be quite reasonably approximated by a linear fit, although a weak but present hysteresis behavior is present. As discussed before, the strong variability represented by the σ standard deviation of dv/v is related to the changes in dominant modes of Rayleigh waves within the studied time window considered for dv/v computations, according to offset. Fig. 11(b) represents the average sensitivity of the dv/v (mean $\pm 1\sigma$) to the water table changes when measured on the time window and on the offsets where only *P*-wave refracted arrivals are present, that is from

60 to 400 m (Fig. 9b). Again, we approximate the relation with a linear fit, neglecting the hysteresis behavior of the curve. The slope of the best linear fit is 10.61 ± 0.1, that is the *P*-refracted wave is roughly 10 times less sensitive to the water table changes than the surface waves are. This weak sensitivity is explained by the low impact of water level variations on the raypaths of the refracted wave when large offsets are considered. Indeed, the refracted waves propagate mainly in the fast velocity layer that constitutes the saturated part. Similarly to the previous analysis, the uncertainties are quite large, and increase for the extrema of the water table, potentially leading to important errors in the interpretation of the depth of the water table. This variability is due to the influence of the refracted *S* wave in this frequency range and in the considered time window, which varies according to the offset.

5 CONCLUSIONS

We confront seismic noise monitoring of water table variations results with numerical simulations of wave propagation built in order to mimic the experiment. To better understand the composition of the seismic wavefield present in the correlogram, we performed active seismic measurements, which allowed us to propose a realistic 1-D elastic model of the subsoil and consequently to simulate the propagation of seismic waves through it. These active and numerical approaches made possible the identification of two dominant Rayleigh modes (fundamental and first higher mode) whose relative amplitude varies with offset. By following a poroelastic approach that quantified the impact of saturation on seismic velocities, we were able to reconstruct a synthetic seismic correlogram that well reproduces the experimental one as well as the velocity variations, which present an anticorrelation with water table changes. We could then assess the offset dependency of velocity variations, highlighting 20 per cent of precision variability due to mode mixing. Finally, the numerical computations indicates that volume waves can be used to track water table changes, particularly when a refracted *P* wave at the water table is singled out in the analyses thanks to an adapted time window selection. The latter provides then a correlation with the water table variations, which has been then quantified. From these results, the seismic noise experiment data have been reconsidered and a correlation between the velocity variations computed from the first arrivals—exhibiting a very poor signal-to-noise ratio—and the water table variations could be established. With the same noise data, the fact that it is possible to establish opposite variations according to the waves analysed, reinforces the interpretation that observed changes are due to fluid substitution processes, here water table variations.

From this study, several aspects would deserve to be developed in the near-future. On the numerical side, it would be important to take into account space variability of geological formations and water content, which should modify the propagation of waves and consequently the offset sensitivity. In particular, formations with localized flow paths such as fractures or karstic zones could be modelled to evaluate the potential of seismic noise based techniques to image and monitor these flow paths of crucial importance in reservoir management. Another benefit would be to upgrade the synthetic viscoelastic computations considering a multiphasic poroelastic approach, where attenuation effects are directly taken into account from the microscale properties with fluid substitution effects included. It should help to better understand amplitude variations observed the data as well as the impact of attenuation variations on the measured velocity variations for the different waves analysed. Finally this study opens the way to denser experiments with a 3-D receivers configuration, which is now possible with the progress in autonomy of the seismic sensors technology. Such experiments should be conducted with three-component sensors so that cross-correlation analyses performed between components could provide more local information derived from the ellipticity properties of surface waves and Love waves could be considered.

ACKNOWLEDGEMENTS

This work is supported by a grant from Labex OSUG@2020 (Investissements d'Avenir - ANR10 LABX56). The authors thank the 'Plateforme de recherche de Crépieux-Charmy', the 'Métropole Grand Lyon' and the society 'Eaux du Grand Lyon' for granting access and support for the experiments. Authors would like to thank Marine Denolle and an anonymous reviewer for their constructive comments on the paper.

REFERENCES

Bianchi, T., Forgues, E., Meunier, J., Huguet, F. & Bruneau, J., 2004. Acquisition and processing challenges in continuous active reservoir monitoring, *Soc. Explor. Seismol., Expanded Abstracts,* **23,** 2263.

Biot, M., 1962. Mechanics of deformation and acoustic propagation in porous media, *J. Appl. Phys.,* **33**(4), 1482–1498.

Bouchon, M., 1981. A simple method to calculate green's functions for elastic layered media, *Bull. seism. Soc. Am.,* **71,** 959–1971.

Campillo, M. & Paul, A., 2003. Long-range correlations in the diffuse seismic coda, *Sciences,* **299,** 547–549.

Clements, T.H. & Denolle, M.A., 2018. Tracking groundwater levels using the ambient seismic field, *Geophys. Res. Lett.,* **45,** 6459–6465.

Demanet, D., Renardy, F., Vanneste, K., Jongmans, D. & Meghraoui, M., 2001. The use of geophysical prospecting for imaging active fault in the roer graben, belgium, *Geophysics,* **66,** 78–89.

Dietrich, M., 1988. Modeling of marine seismic profiles in the t-x and $\tau - p$ domains, *Geophysics,* **53,** 453–465.

Dines, K. & Lyttle, J., 1979. Computerized geophysical tomography, *IEEE,* **67**(7), 1065–1073.

Dupuy, B., Garambois, S., Asnaashari, A., Balthareth, H., Landro, M., Stovas, A. & Virieux, J., 2015. Estimation of rock physics properties from seismic attributes. Part I: strategy and sensitivity analysis, *Geophysics,* **81**(3), M35–M53.

Fores, B., Champollion, C., Mainsant, G., Albaric, J. & Fort, A., 2018. Monitoring saturation changes with ambient seismic noise and gravimetry in a karst environment, *Vadose Zone J.,* **17**(1), doi:10.2136/vzj2017.09.0163.

Garambois, S. & Dietrich, M., 2002. Full waveform numerical simulation of seismoelectromagnetic wave conversions in fluid-saturated stratified porous media, *J. geophys. Res.,* **107**(B7), ESE 5–1-ESE 5-18.

Garambois, S., Sénéchal, P. & Perroud, H., 2002. On the use of combined geophysical methods to assess water content and water conductivity of near-surface formations, *J. Hydrol.,* **259,** 32–48.

Grêt, A., Snieder, R. & Scales, J., 2006. Timelapse monitoring of rock properties with coda wave interferometry, *J. geophys. Res.,* **111**(B3), doi:10.1029/2004JB003354.

Kennett, B.L.N. & Kerry, N.J., 1979. Seismic waves in a stratified half space, *Geophys. J. R. astr. Soc.,* **57,** 557–583.

Larose, E. *et al.* 2015. Environmental seismology: what can we learn from ambient noise? *J. appl. Geophys.,* **116,** 62–74.

Lecocq, T., Longuevergne, L., Pedersen, H.A., Brenguier, F. & Stammler, K., 2017. Monitoring ground water storage at mesoscale using seismic noise: 30 years of continuous observation and thermo-elastic and hydrological modeling, *Scient. Rep.,* **7,** 14241.

Lobkis, O.I. & Weaver, R.L., 2001. On the emergence of the green's function in the correlations of a diffuse field, *J. acoust. Soc. Am.,* **110**(6), 3011–3017.

Loizeau, S., 2013, Amlioration de la comprhension des fonctionnements hydrodynamiques du champ captant de crépieux-charmy, *PhD thesis*, University of Grenoble, France, p. 220.

Pasquet, S., Bodet, L., Dhemaied, A., Mouhri, A., Vitale, Q. & Rebiba, D.E.A., 2015. Detecting different water table levels in a shallow aquifer with combined p-, surface and sh-wave surveys: insights from v p /v s or poisson's ratios, *J. appl. Geophys.,* **113,** 38–50.

Réfloch, A., 2018, Compréhension expérimentale et numérique des chemins de l'eau sur l'ensemble du champ captant de la métropole de lyon, *PhD thesis*, University Grenoble Alpes, p. 262.

Sambridge, M., 1999a. Geophysical inversion with a neighbourhood algorithm – I. Searching a parameter space., *J. geophys. Int.,* **138,** 479–494.

Sambridge, M., 1999b. Geophysical inversion with a neighbourhood algorithm – II. Apprising the ensemble., *J. geophys. Int.,* **138,** 727–746.

Schuster, G.T., 2009. *Seismic Interferometry,* Cambridge University Press.

Sens-Schoenfelder, C. & Wegler, U., 2006. Passive image interferometry and seasonal variations of seismic velocities at merapi volcano, indonesia, *Geophys. Res. Lett.,* **33**(L21302), 1–5.

Tsai, V.C., 2011. A model for seasonal changes in gps positions and seismic wave speeds due to thermoelastic and hydrologic variations, *J. geophys. Res.,* **116,** B04404.

Voisin, C., Garambois, S., Massey, C. & Brossier, R., 2016. Seismic noise monitoring of the water table in a deep-seated slow-moving landslide, *Interpretation,* **4,** SJ67–SJ76.

Voisin, C., Guzman, M., Réfloch, A., Taruselli, M. & Garambois, S., 2017. Groundwater monitoring with passive seismic interferometry, *J. Wat. Resour. Protect.,* **9,** 1414–1427.

Wathelet, M., Jongmans, D. & Ohrnberger, M., 2004. Surface wave inversion using a direct search algorithm and its application to ambient vibration measurements, *Near Surf. Geophys.,* **2,** 211–221.